nature communications

Article

https://doi.org/10.1038/s41467-026-68767-9

A Magnon-photon interface based on Van der Waals Magnetic semiconductor

Received: 30 May 2025

Accepted: 16 January 2026

Qian Hu[1,2], Yuqing Huang[1,2] ✉, Jiangang Feng[3,4] ✉, Antonio Fieramosca[5], Hui Wen[1,2], Xiaomin Zhang[1], Wenkai Zhu[1], Ninghua Jiang[1,2], Xuan Qian[1,2], Jing Zhang[1,2], Yang Ji[6], Daniele Sanvitto[5] & Kaiyou Wang[1,2] ✉

Coherent control of light with electron spins represents a fundamental goal across multiple research fields, such as opto-spintronics, chiroptics, quantum information. In a magnetic-ordered material, coherent magnon gives rise to temporally and spatially modulated spin structure that may stimulate intriguing spin-photon interactions as well as opto-spintronic applications. However, the development of such magnon-photon interface is hampered due to the lack of magnetic photonic structure that embraces strong light-matter interaction. Here, we present such magnon-photon interface in a CrSBr metasurface by showing the formation of a magnetic exciton polariton bound states in the continuum, whose energy and the radiative properties can be tuned with an external magnetic field. We further show that the exciton polaritons are modulated by the coherent magnon excitation, exhibiting a nontrivial magnon mode- and k-dependent behavior which suggests the formation of hybrid magnon-exciton polariton states. Our results shed light on the interplay of spin, magnon and photon in the magnetic metasurface and provide a new platform for exploring spin functional photonic and quantum devices.

The electron spin carries non-volatile quantum information, which has been widely explored for information storage and processing[1–5]. Interfacing the spin states with photons allows communication and detection of spin quantum information over long distance[6–9]. Such spin-photon interface is therefore critical to connecting spatially separated quantum nodes and has been recognized as a vital part of the vision for scalable spin quantum information.

Significant progress has been made for non-magnetic spin-photon interface. This includes development of high-fidelity spin-photon entangled states, photon switches, routers and efficient chiral emitters controlled by electron spin in III-V semiconductor quantum dots[7,9,10], transition metal dichalcogenide[11–13] as well as scalable on-chip integration of optically active defect spins in diamond and SiC[8,14,15]. The non-magnetic semiconductor nanostructures and color centers are benefited from the optically active materials and long spin coherence time[16,17]. Whereas, magnetic materials, although being the backbone of contemporary spintronic research and memory industry, are less explored due to optically inactive band-edge transitions[18,19], degraded optical properties[20,21], as well as limited spin relaxation and coherence time[22,23].

Recently, the discovery of magnetic semiconductors, e.g., CrSBr, with strong light-matter interaction and intriguing magneto-electronic

---

[1]State Key Laboratory of Semiconductor Physics and Chip Technologies, Institute of Semiconductors, Chinese Academy of Sciences, Beijing, China. [2]College of Materials Science and Opto-Electronic Technology, University of Chinese Academy of Sciences, Beijing, China. [3]School of Chemistry and Materials Science, University of Science and Technology of China, Hefei, China. [4]Suzhou Institute for Advanced Research, University of Science and Technology of China, Suzhou, China. [5]CNR NANOTEC Institute of Nanotechnology, Lecce, Italy. [6]School of Physics, Zhejiang University, Hangzhou, China.
✉e-mail: yqhuang@semi.ac.cn; jgfeng@ustc.edu.cn; kywang@semi.ac.cn

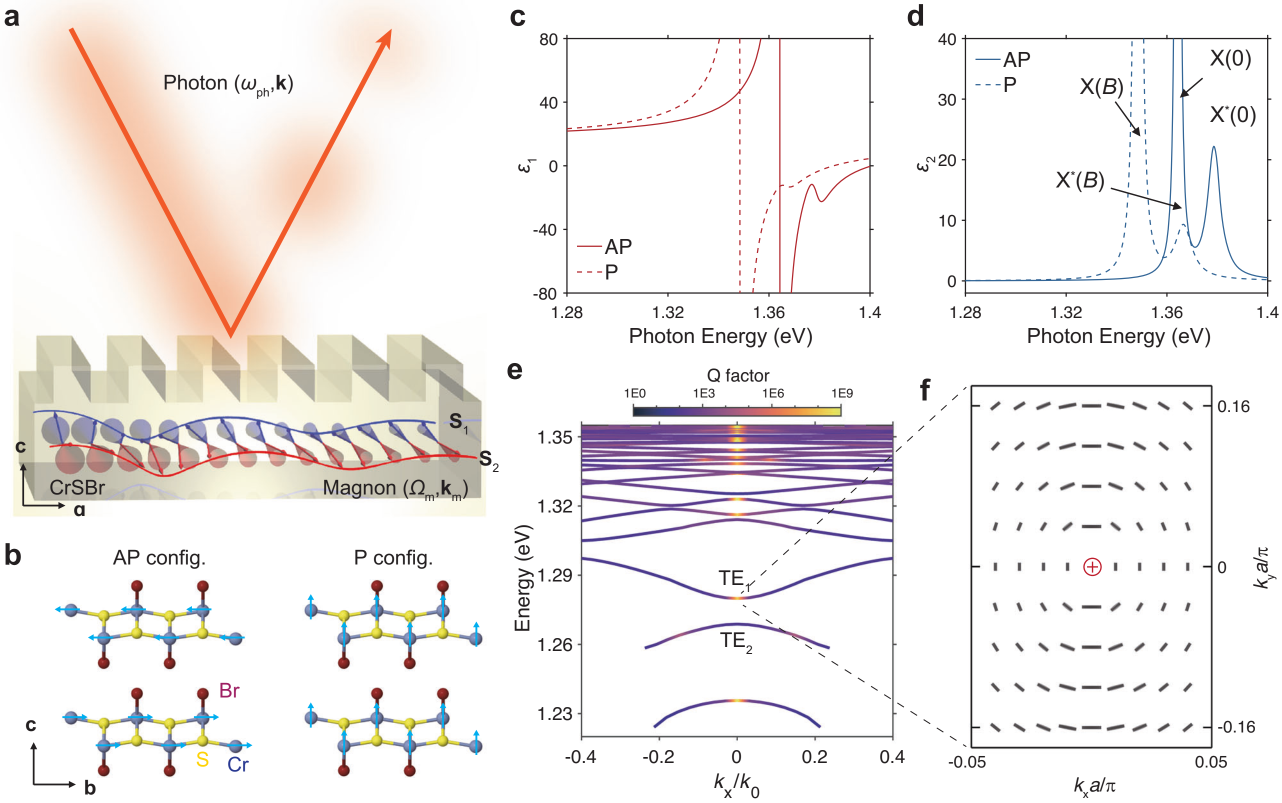

Fig. 1 | Magnon-photon interface combining magneto-optical effect and photonic BICs. a Schematic illustration of the CrSBr metasurface as the magnon-photon interface. Photon with given ω_{ph} and **k** is reflected and modulated by the coherent magnons with frequency Ω_m and $\mathbf{k}_m$. $\mathbf{S}_1(t)$ and $\mathbf{S}_2(t)$ represent the anti-ferromagnetically coupled macrospins in the adjacent layers of CrSBr. **b** Illustration of the interlayer parallel (P) and anti-parallel (AP) spin configuration of CrSBr. **c**, **d** *b*-axis dielectric function $\varepsilon_b = \varepsilon_1 + i\varepsilon_2$ of CrSBr for P and AP spin configuration. The data is extracted from the reflectance spectra of a 150-nm-thick CrSBr flake. **e** The simulated TE mode and Q factor for a free-standing 1D CrSBr grating in the spectral range of the lower exciton polariton. The BICs mode TE_1 is marked. The imaginary part of ε_b is omitted in the calculation. **f** Far-field polarization map of the TE_1 mode in (**e**) which highlight an on-Γ BICs mode with topological charge $C = +1$.

coupling effect has revived the hope for developing a spin-photon interface that allows harvesting the versatility of spin manipulation and magnetic phase engineering in a magnetic material[24–30]. Additionally, magnon arises as a unique wave-like spin excitation in magnetically ordered materials[31]. In CrSBr, magnon is found strongly coupled to the excitonic states, reshaping its optical properties in the ultrafast time scale[32,33]. Despite the development, two major obstacles persist. First of all, studies of magnon-exciton interactions in 2D magnetic semiconductors have only been conducted in structureless samples which mostly involving interaction with free-space photons. Carefully designed photonic structures, e.g., photonic cavity or metasurfaces with high quality factor or strong magneto-optical response, will likely not only enhance the spin-photon interaction but also provide extra tunability[34–36]. In particular, photonic structures hosting bound states in the continuum (BICs) have attracted great attention due to their potential to achieve infinite-high cavity Q factors and sensitive to external perturbations, giving rise to intriguing light-matter interaction that facilitate the low threshold lasing, ultrafast optical switches, etc[37–39]. Coupling of the non-local BICs mode with the local excitation in the magnetic materials, e.g., excitons, may also give access to significant tunability through interplay of the local and non-local transition of the system[40,41]. Secondly, the fundamental physics underlying the coupling between collective spin waves and photons is not well understood. Although the propagation of magnons in CrSBr has been confirmed[42,43], its interaction with the excitonic states is probed in a momentum-integrated manner. A momentum-resolved perspectives are therefore highly appreciated to shed light on the exotic nature of the magnon-photon coupling.

In this work, we demonstrate a magnon-photon interface based on a 1D metasurface of the magnetic semiconductor CrSBr. The CrSBr metasurface hosts BICs that are strongly coupled with excitons forming exciton polaritons (EPs). Owing to the magneto-electronic coupling effect of CrSBr and photonic singularity of the BICs mode, both the energy and the reflectivity of the half-light, half-matter state can be efficiently tuned with an external magnetic field. Furthermore, by performing the transient angle-resolved reflectance spectroscopy on the CrSBr metasurface, we find that the coherent magnon introduces a non-trivial k-dependent oscillation of EP energies that behaves differently for acoustic and optical magnons. These results highlight the wave nature of the magnon-photon coupling in the CrSBr metasurface, which establishes an innovative approach for controlling the photonic or polaritonic devices with electron spins.

Results

Magnon-photon interface combining magneto-optical effect and photonic BICs

Figure 1a illustrates the proposed magnon-photon interface made from a CrSBr grating, in which the reflected light of frequency ω_{ph} and momentum **k** is coupled to the transverse electric (TE) mode of the grating and is modulated by a launched coherent magnon. The bulk CrSBr is an A-type antiferromagnetic semiconductor with Néel temperature $T_N = 132$ K. The orientation of the antiferromagnetically coupled macrospins $\mathbf{S}_1$ and $\mathbf{S}_2$ in the adjacent layers has strong impact

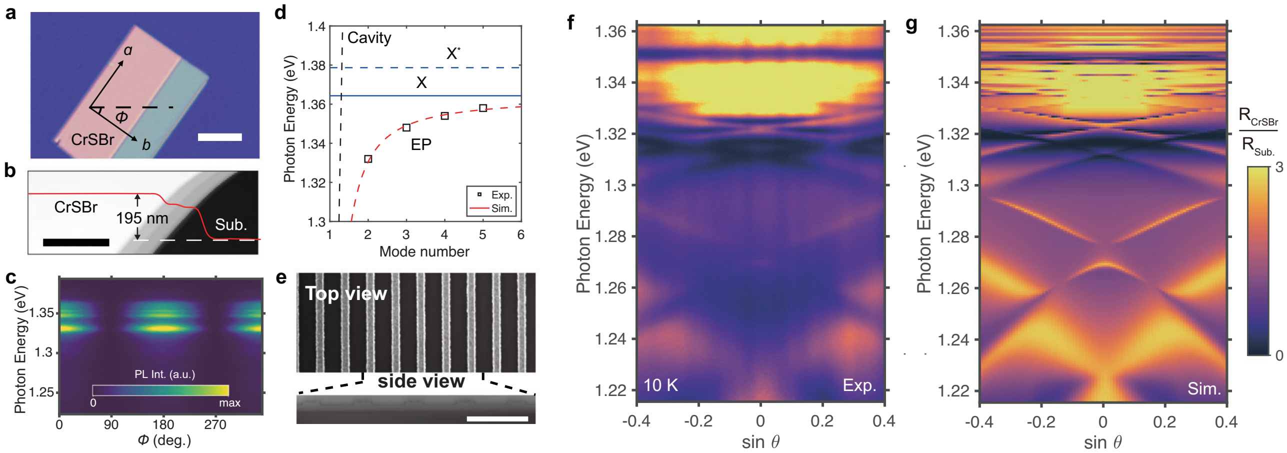

Fig. 2 | **Fabrication and characterization of the CrSBr metasurface. a** Optical image of mechanically exfoliated CrSBr flake. The crystallographic axis is marked. **b** The AFM image of the CrSBr flake. The height profile is shown as red line. **c** PL spectra as the function of the detection linear polarization angle ϕ with respect to the b-axis. **d** PL peak position of a 150-nm CrSBr flake is plotted as function of FP cavity mode number. The peak position fits to the simulated EP energy using coupled oscillator model (red dashed line). The energy of excitonic states (X^* and X) and cavity is also shown. **e** Top and side view SEM images of a CrSBr metasurface. **f**, **g** are the measurement and simulation of Angle-resolved reflectance spectra from the CrSBr gratings with grooves parallel to b-axis. The measurements are carried out for s polarized configuration. The PL and reflectance measurement are carried out at 10 K. The scale bars in (**a**, **b** and **e**) are 50 μm, 3 μm and 1 μm respectively.

on the excitonic structure as well as optical response of the material. By applying an external magnetic field of $B = 3$ T along the c-axis, $\mathbf{S}_1$ and $\mathbf{S}_2$ switch from anti-parallel (AP) to parallel (P) spin configuration as shown in Fig. 1b. As a result, the b-axis dielectric function $\varepsilon_b = \varepsilon_1 + i\varepsilon_2$ of CrSBr is modified drastically as shown in Fig. 1c, d. Here, ε_b is extracted from the reflectance spectra with details given in Supplementary Note 1 and Fig. S1. The multi-resonance reflectance features in Fig. S1 is due to the multi-order Fabry-Perot resonances arise from the planar cavity formed between the top and bottom surface of the CrSBr flake and is therefore not reflected by the fitted ε_b in Fig. 1c, d. The giant magneto-optical response is caused by spin mediated interlayer coupling, leading to a prominent redshift of the 1s exciton state from $X(0) = 1.3643$ eV to $X(B) = 1.3485$ eV as marked in Fig. 1d. Such magneto-electronic effect stems from the exchange interaction and is expected to have a stronger impact than typical magneto-optical effects, e.g., Faraday, Kerr rotation, etc., which are received from the spin orbital interaction[44]. In Fig. 1e, we show the calculated TE mode dispersion of the proposed CrSBr grating. Owing to the strong light-matter interaction, the shown eigen modes are essentially EPs hybridized between the 1s exciton and guided resonances (GRs). The Γ point of the TE_1 mode as marked in Fig. 1e is a BICs with topological charge $C = +1$, evidenced by divergent Q factor and the far-field polarization map as shown in Fig. 1f. The corresponding mode distribution can be found in Supplementary Fig. S2. The BICs mode is often considered as photonic singularity which is inherited with strong tunability. However, to our knowledge, its role in a magnetic metasurface as the one shown here has not yet been explored.

Strong coupling of exciton and BICs mode in a CrSBr 1D grating

The optical and atomic force microscopy (AFM) image of the exfoliated CrSBr flake is shown in Fig. 2a, b. The polarization-resolved photoluminescence (PL) spectra in Fig. 2c reveals emissions from a series of self-hybridized EPs that are linearly polarized along the b-axis. The coupling strength is estimated to be ~ 167 meV by fitting the emission peak position with a coupled oscillator model (COM) as shown in Fig. 2d (see Supplementary Note 2 and Fig. S3).

Next, the CrSBr metasurface is fabricated by patterning the CrSBr flakes with e-beam lithography followed by dry etching. The grating grooves are aligned along the b-axis of the crystal to maximize the coupling strength. In Fig. 2e, the scanning electron microscope (SEM) image shows that the bottom part of the CrSBr flake is still connected, allowing the continuous propagation of spin wave throughout the whole structure. Figure 2f shows the angle-resolved reflectance (ARR) spectrum taken from the CrSBr metasurface at 10 K, which is nicely matched to the simulated ARR spectrum in Fig. 2g. In Supplementary Fig. S4, we show the ARR spectrum from a CrSBr metasurface with the same structure parameters while the grating grooves are along a-axis. In this case, the photonic modes are decoupled from the exciton, giving rise to markedly different dispersion as in Fig. S4. Furthermore, we have carried out analysis based on COM and the simulation results are shown in Fig. S5. The COM suggests that a coupling strength of ~ 186 meV is needed to reproduce the observed polariton dispersion and the strong coupling is also reached in the CrSBr grating sample. We note that the slightly increase of the fitting values for the coupling strength as well as exciton oscillator strength (see table S1) for the CrSBr grating as compared to the bulk sample is likely artificially caused by the Lorentzian dielectric model[25,26] which neglects the energy dependence of the background dielectric constant ε_{b0}. A more accurate determination of the coupling strength requires a more realistic modeling of the dielectric function over large spectral range. Nevertheless, the obtained comparable exciton oscillator strength for the etched and unetched sample suggests that the optical quality of the CrSBr grating is not compromised by etching. The EPs at around 1.27 eV in Fig. 2f features a bright and dark state (BS and DS) at Γ point ($\theta = 0$) separated by a gap of ~8 meV. The same spectral feature is observed in the angle-resolved PL (ARPL) spectrum in Fig. 3a. The EPs emission intensity diminishes at the vicinity of the DS, accompanied by the increase of the Q factor as shown in Fig. 3b. The DS and BS are identified as the TE_1 and TE_2 EP. The two modes are slightly redshifted compared from the eigen mode calculation in Fig. 1e due to the presence of the SiO_2/Si substrate. The absence of the PL and reflectance contrast of the DS is due to the symmetry-forbiden emission of the BICs at $\theta = 0°$. In the following content, we will refer to the exciton polariton formed by the strong coupling between the BICs mode and CrSBr excitons as EP BICs for short.

Tuning the exciton polariton BICs with magnetic field

The formation of EP BICs facilitates the control of its optical response by manipulating the spin configuration. Applying an out-of-plane magnetic field tilts the macrospins $\mathbf{S}_1$ and $\mathbf{S}_2$ as illustrated in Fig. 3c.

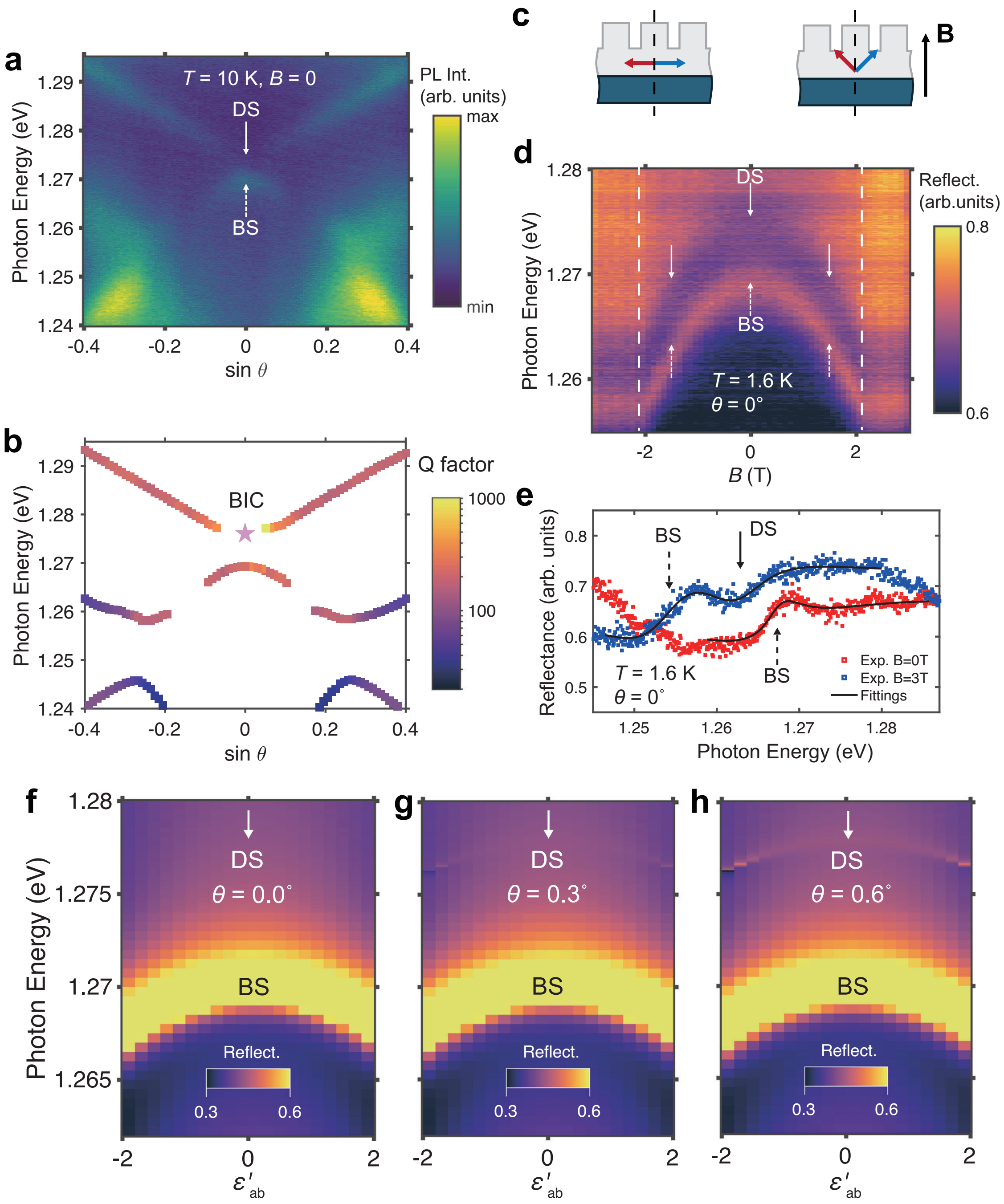

Fig. 3 | Formation and controlling of the magnetic EP BICs in CrSBr metasurface. a ARPL spectra of the CrSBr metasurface measured without magnetic field. The Γ point bright (BS) and dark (DS) state are marked. **b** The fitted energy position and Q factor of the EP emission from the ARPL in **a** are plotted as function of θ. **c** Schematic illustration of canting of the interlayer macro spins in the presence of magnetic field. **d** ARR spectra of CrSBr metasurface at $\theta = 0^\circ$ are plotted as function of out-of-plane magnetic field. The redshift and emerging of the DS reflection is marked in solid arrow. **e** Comparison between the reflectance spectra of the CrSBr metasurface at $\theta = 0^\circ$ for $\mathbf{B} = 0$ and 3 T. The spectra are fitted with Fano lineshape and the spectra feature for DS and BS is marked. Simulations of the ARR spectra at Γ ($\theta = 0^\circ$ in **f**) and near Γ ($\theta = 0.3^\circ$ and 0.6° in **g**, **h**) show the reflectance contrast of the quasi-BICs is strongly modified with ε'_{ab} within angle uncertainty $\Delta\theta$.

The change of spin configuration modulates the energy of the EPs. As shown in Fig. 3d, the BS redshifts with magnetic field and reaches saturation at $B = 2.1$ T. The total energy change of the BS $\Delta E_{BS} = 13.1$ meV is huge considering the field induced total energy shift of 1 s exciton is about $\triangle E_{ex} = 15.8$ meV. The large energy shift is consistent with the substantial exciton fraction of the EP which is estimated $|X_L|^2/(|X_L|^2 + |C_L|^2) = 0.39$ using the coupled oscillator model. Here, X_L and C_L are the exciton and photon part of the Hopfield coefficients for the lower polariton branch[45].

Interestingly, The EP BICs which is completely dark in the ARR measurement in the absence of magnetic field, start to redshifts and develops a reflectance feature with applying magnetic field. The brightening of EP BICs is further illustrated in Fig. 3e, where two resonant features are identified at $B = 3$ T and fitted with Fano lineshape. The dashed and solid arrows mark the fitted resonant energies of the bright and dark state. Table S2 in the supplementary information summarizes the fitting parameters for the two resonances. As guided by the fitting curves, the dark state locates at about 8 meV above the

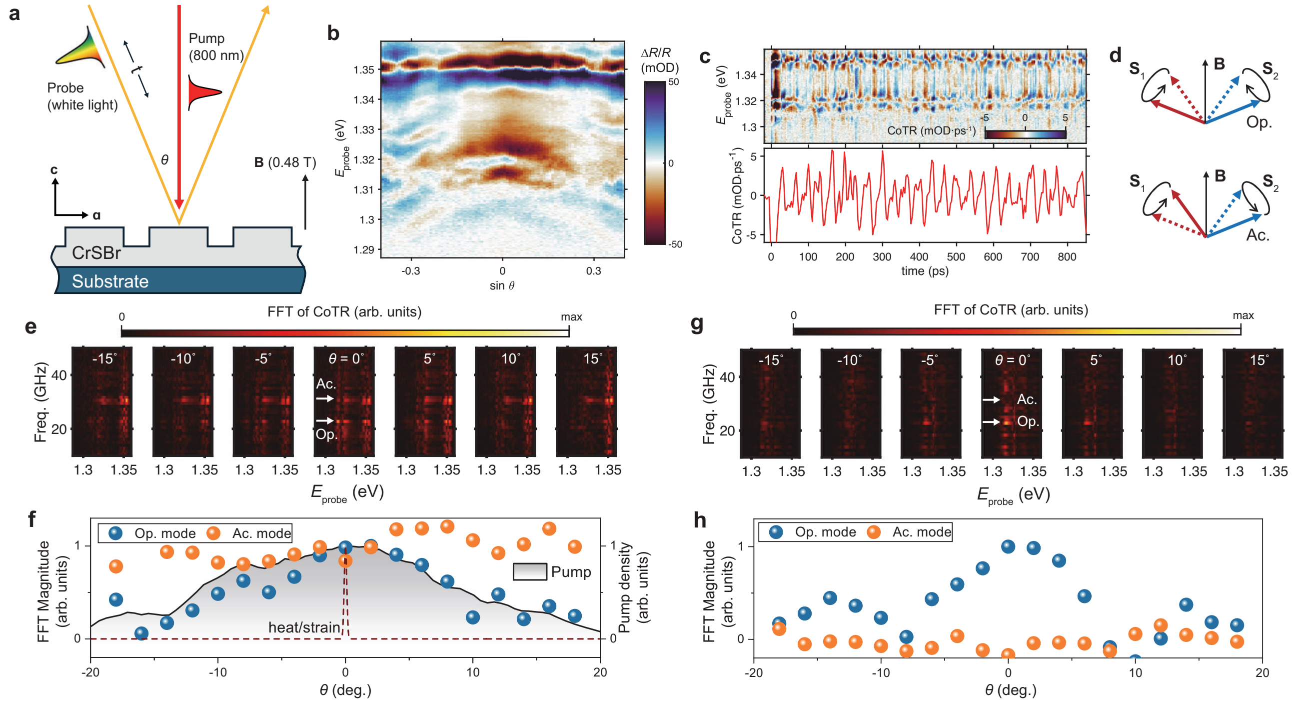

Fig. 4 | Magnon mode- and k-dependent magnon-EP interaction revealed by ultrafast spectroscopy. a Schematics of the tr-ARR measurement. The pump and probe spot size is 10 µm. **b** The tr-ARR signal ΔR/R at pump-probe delay time $t = 47$ ps as function of probe photon energy E_{probe} and θ. **c** Measured coherent oscillation of the tr-ARR (CoTR) for $\theta = 0^{\circ}$ at different E_{probe} (top panel) and a fixed $E_{\mathrm{probe}} = 1.3536$ eV (bottom panel). **d** Schematics of the optical (Op.) and acoustic (Ac.) magnon mode. The former features out-of-phase precession of interlayer macro spin $\mathbf{S}_1$ and $\mathbf{S}_2$, leading to a time-varying angle between $\mathbf{S}_1$ and $\mathbf{S}_2$. In the latter case, $\mathbf{S}_1$ and $\mathbf{S}_2$ precess in-phase and their angle stay constant. **e** FFT spectra of CoTR as function of E_{probe} at different θ for the CrSBr grating. The oscillation frequency of acoustic (Ac.) and optical (Op.) magnon is marked. **f** FFT magnitude at Op. and Ac. magnon frequency is plotted as function of θ for the CrSBr grating. The estimation of the angular profile for strain/heat effect (dashed line) and the normalized k-space distribution of the pump density (solid line with shadow) are also shown. **g** FFT spectra of CoTR as function of E_{probe} at different θ for the unetched CrSBr flake. **h** Angle dependent FFT magnitude at Op. and Ac. magnon frequency for unetched CrSBr flake. All the measurements are conducted at 14 K with an out-of-plane magnetic field 0.48 T.

bright state and exhibits a highly asymmetric lineshape. As a comparison, only the resonant feature of the BS is observed and fitted for spectrum measured at $B = 0$ T in Fig. 3e.

An out-of-plane magnetic field contributes to a sizable off-diagonal dielectric tensor element $\varepsilon_{ab} = \varepsilon'_{ab} + i\varepsilon''_{ab}$ (see Supplementary Note 3 and Fig. S6)[46]. ε_{ab} introduces coupling between GRs and broad FP resonances, that can potentially affects the reflectance spectra in field. Ideally the Γ-point BICs is strictly radiatively forbidden. The robustness of the BICs is protected by the C_2 symmetry which holds even in the presence of magnetic field. This is shown with simulated reflectance spectra in Fig. 3f in which the reflectance features of BICs is absent at different ε'_{ab} for a perfect grating with infinite periods. However, the translation symmetry is broken due to limited sample size or white light spot size. As a result, the reflectance at $\theta = 0^{\circ}$ mixes in the contributions from near-Γ quasi-BICs at finite $\mathbf{k}$. Considering system dimension of ~20 µm limited by beam size, it leads to a k-space blurriness of $\Delta\theta \sim 1.4^{\circ}$ as estimated with the uncertainty relation $\Delta k \cdot \Delta x \geq 1/2$. Such near-Γ contribution is simulated in Fig. 3g, h for $\theta = 0.3^{\circ}$ and 0.6°. It is evident that the reflectance features of the quasi-BICs state (DS) gradually build up with the increase of ε'_{ab} within the uncertainty limit of $\Delta\theta$, which is consistent with the experimental observation of the brightened BICs in Fig. 3d and e. In Fig. S7, we further show from simulation that the field-induced reflectance features from the quasi-BICs depends on both real and imaginary part of ε_{ab} and generally leads to asymmetric Fano lineshape as observed in the experiment. The observed intriguing magneto-optical effect emerges exclusively at the magnetic EP-BICs, which is due to the combined effect of the magnetic field induced ε_{ab} and the fact that the quasi-BICs is sensitive to such external perturbation. In Supplementary Fig. S8, as a comparison, we show that the reflectance amplitude is barely changed for other EPs that are far apart from the BICs point.

k-dependent magnon-exciton polariton interaction

Next, we turn to the EPs that are closer to the exciton resonance which maximize the magnon-photon interaction. A transient ARR (tr-ARR) spectroscopy is employed to study the interaction between the EPs and coherent magnons in the CrSBr metasurface. The tr-ARR monitors the time evolution of the pump induced ARR change $\Delta R/R(\theta, E_{\mathrm{probe}})$ which are function of both the probe light energy E_{probe} and θ. Our measurement configuration is shown in Fig. 4a. A constant magnetic field of 0.48 T is applied to cant the interlayer spins which facilitate exciton-magnon coupling[25]. Figure 4b shows a typical tr-ARR spectrum measured at 14 K and $t = 47$ ps. Here, the $\Delta R/R$ is mainly caused by pump induced redshift of the EPs, which is opposite to the typical blueshift observed for EPs nonlinearity in non-magnetic materials[47,48]. The effect is pronounced for EPs derived from the FP mode at around 1.35 eV and multiple GRs in between 1.3-1.34 eV. We attribute the $\Delta R/R$ signal to the excitation of incoherent magnon, which contributes to the decreases of EP energies and decays slowly with time as shown in Supplementary Fig. S9. Apart from the incoherent component, the coherent magnon excitation is also observed as the temporal oscillation of the $\Delta R/R$. In the upper panel of Fig. 4c, the coherent oscillation of the tr-ARR (CoTR) is made pronounced by taking the time derivative of $\Delta R/R$ and is plotted as function of E_{probe} and t for $\theta = 0^{\circ}$. The oscillations take opposite phase for E_{probe} above and below the EP resonances. It suggests that the EP energies are periodically modulated

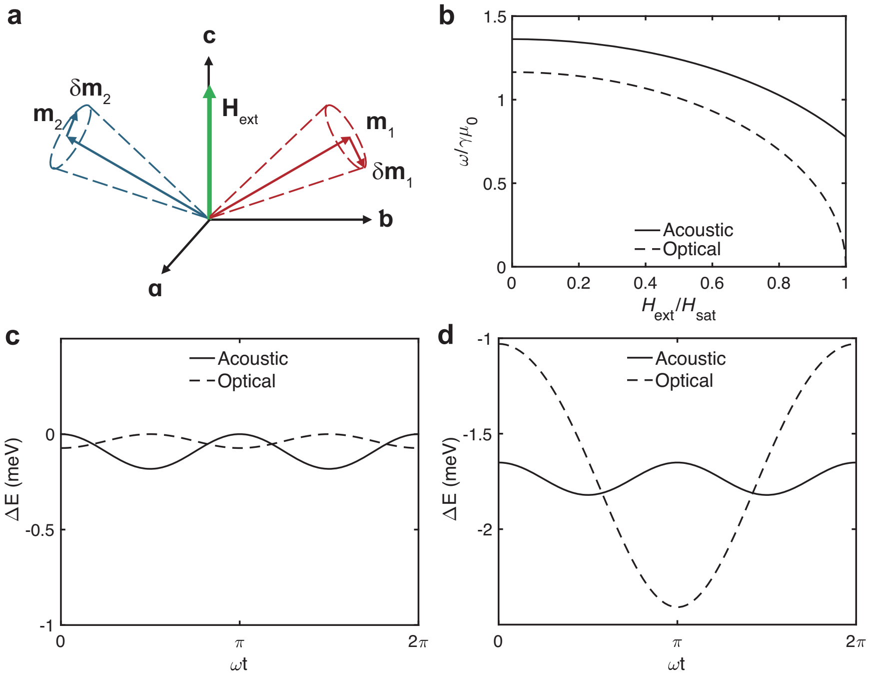

Fig. 5 | Simulation of the optical and acoustic magnon modes in bulk CrSBr. **a** Illustration of the sublattice spin orientation $\mathbf{m}_1$ and $\mathbf{m}_2$ of CrSBr in the precense of magnetic field strength $H_{\rm ext}$. **b** Simulation of the magnon frequency as function of $H_{\rm ext}$. The saturation magnetic field $\mu_0 H_{\rm sat} = 2.1$ T is assumed. **c**, **d** Simulation of the temporally modulated exciton energy due to the coherent magnon excitation for acoustic and optical magnon modes at $\mu_0 H_{\rm sat} = 0$ and 0.48T. The magnon spin precession amplitude is set to $|\delta\mathbf{m}_1| = |\delta\mathbf{m}_2| = 0.1$.

through interaction with coherent magnon, which is consistent with previous report in pristine CrSBr flakes[32]. In the lower panel of Fig. 4c, CoTR at probe energy ($E_{\rm probe} = 1.3536$ eV) slightly above the 1.35-eV EP is plotted against time, exhibiting clear oscillations with a beating amplitude.

To gain in-depth understanding of the coherent magnon-EP dynamics, we performed fast Fourier transformation (FFT) of the CoTR signal for each $E_{\rm probe}$ and the results for different θ are shown in Fig. 4e. In the FFT spectra, two dominant oscillation frequencies at 30 GHz and 22 GHz are identified and attributed to the acoustic and optical magnon modes (marked as Ac. and Op.). The corresponding mode character featured by the in-phase and out-of-phase precession of the macrospin $\mathbf{S}_1$ and $\mathbf{S}_2$ of the neighboring antiferromagnetically coupled layers is illustrated in Fig. 4d. In Fig. 4f, the FFT magnitude at the two magnon mode frequencies is plotted against θ. The FFT magnitude at the frequency of optical magnon decreases at higher $|\theta|$, whereas the acoustic magnon contribution remains at a comparable level for all θ in our measurements. The k-dependent coupling between EP and optical magnon can not be explained by any k-space dispersion of the EP, which would otherwise create similar angle-dependent trend for both magnon modes.

It has been suggested that the transient strain field generated by the pump light plays important roles for launching magnon in CrSBr and the k-space distribution of the coherent magnon should be limited by the Fourier transformation of the real-space transient strain field[42]. In our measurement, the pump laser was defocused to a large laser spot size of ~10 μm. It therefore generates a broad real-space heat/strain profile. The dashed line in Fig. 4f estimate the contribution of heat/strain by showing the Fourier transformation of the real-space laser spot profile, which is too narrow to account for the observation of the broad k-space profile for the optical magnon. It suggests that the magnon mode- and k-dependent coherent magnon-EP oscillations observed here are beyond the conventional heat/strain-mediated mechanism which is often responsible for magnon-photon interaction in magnetic materials or devices. Furthermore, the optical magnon has a similar profile as the angular distribution of the pump density (Fig. 4f). It is worth to know that such angular distribution of the pump density deviates from the Fourier transformed real-space profile of the pump beam due to the defocused pump laser beam setting. This is a strong indication for a k-conserved coupling between EP and the optical magnon such that the momentum is transferred to the magnon mode upon optical excitation. However, such momentum conservation law does not hold for acoustic magnons. We note that the similar k-conserved behavior of the optical magnon is also observed for measurement in pristine CrSBr as shown in Fig. 4g, h. However, a noteworthy difference in the unpatterned CrSBr is that the acoustic mode is absent in the FFT spectra at all angles.

To shed light on the different k-space behavior of the optical and acoustic magnons, we solved the Landau-Lifshitz equation describing the time evolution of sublattice magnetization $\mathbf{m}_{i=1,2}(t)$ of bulk CrSBr as illustrated in Fig. 5a,

$$\frac{\mathrm{dm}_i(t)}{\mathrm{d}t} = -\gamma\mu_0 \mathrm{m}_i(t) \times \mathrm{H}_{i,\mathrm{eff}} \tag{1}$$

Here, γ and μ_0 are gyromagnetic ratio and vacuum permeability. $\mathbf{H}_{i,\rm eff}$ is the effective magnetic field of $\mathbf{m}_{i=1,2}(t)$ and includes contributions from Zeeman interaction, interlayer exchange coupling and the magnetic anisotropy (detailed derivation is given in Supplementary Note 4). Assuming the reported interaction parameters, Fig. 5b shows the calculated mode frequencies for acoustic and optical magnons as function of the c-axis magnetic field[32]. It is established that the modulation of the CrSBr exciton and exciton polariton energies ΔE is proportional to the relative angle between $\mathbf{m}_1(t)$ and $\mathbf{m}_2(t)$ following $\Delta E = \Delta E_{\rm ex}\mathbf{m}_1(t)\cdot\mathbf{m}_2(t)/|\mathbf{m}_1(t)||\mathbf{m}_2(t)|$. Here, $\Delta E_{\rm ex}$ is the exciton energy difference between ferromagnetic and antiferromagnetic phase. Figure 5c, d calculate the temporal modulation of ΔE at zero and finite magnetic field assuming either acoustic or optical magnon is excited. At $H_{\mathrm{ext}} = 0$, neither acoustic nor optical magnon is coupled to the exciton or EPs, as evidenced by the absence of ΔE at the magnon frequency ω in Fig. 5c. However, weak higher order frequency component at 2ω is identified for both magnons. A finite magnetic field, e.g., $\mu_0 H_{\mathrm{ext}} = 0.48$ T, iniates the coupling between the exciton and the optical mode as shown by the emerging oscillation of ΔE at ω in Fig. 5d. Whereas, the acoustic mode remains decoupled at frequency ω. Such distinct selection rules for acoustic and optical magnons in bulk CrSBr nicely explain the absence of the acoustic magnon in the FFT spectra for the unetched CrSBr sample (Fig. 4g, h). The observation of disallowed acoustic magnon in the FFT spectra for CrSBr grating (Fig. 4e, f) then must arise from the etched edges and sidewalls which have low symmetry. At such localized site, the acoustic magnon-exciton polariton interaction therefore does not conserve **k** and naturally leads to an insensitive dependence on angle. On the other hand, the selection-rules-allowed optical mode requires match of momentum owing to the preserved translation symmetry and therefore leads to an angle-sensitive behavior for both the pristine CrSBr flake and the CrSBr grating. The mode- and k-dependent magnon-EP interaction may indicate the formation of strongly coupled EP-magnon hybrid such that a k-selected excitation of the EPs directly leads to the k-dependent pumping of the coherent magnons which in turn modulates the EPs energies.Such mechanism is therefore sensitive to the character of the magnons in the way that favors the direct optical magnon-EP coupling through the induced angle change between adjacent interlayer macrospins.

We note that controlling light with electron spins has strong implications in spin quantum information and spintronics, which is generally difficult for conventional meta-surfaces or polaritonic devices based on non-magnetic materials. Towards such goal, we have demonstrated both static and ultrafast control of exciton polariton with electron spin or collective modes of spins in a magnetic photonic structure of CrSBr, by harnessing the synergistic interplay between strong light-matter interactions and magneto-electronic effect in the 2D magnetic semiconductor. More importantly, the observation of magnon mode- and k-dependent magnon-EP interaction provides a compelling evidence of direct momentum transfer from pump photons to the optical magnons, suggesting the formation of strongly coupled magnon-EP hybrid state. These findings provide valuable information for the spin- and magnon-photon interactions in the 2D limit and open a new gateway for exploring spin functional photonic and quantum devices with 2D magnetic semiconductors.

Methods

Fabrication of CrSBr metasurface

The commercially available CrSBr crystal (from Nanjing MKNANO) was mechanically exfoliated onto a silicon substrate with a 300-nm oxide layer in the glove box, and the thickness was determined using AFM. Electron beam lithography and ICP-RIE were used to partially etch CrSBr, forming a one-dimensional grating. The etched area of the CrSBr flake is 30 μm × 30 μm. The grating structural parameters and roughness of the measured grating sample is characterized by SEM and AFM in Fig. S10.

Angle-resolved reflectance and PL spectroscopy

The optical measurements are conducted with samples loaded into a low-vibration closed-cycle cryostat. For the PL measurement, a 532-nm continue-wave laser was used for excitation. A halogen lamp was used for the reflectance measurement. The PL emission and the reflected light were collected with a long-working-distance objective lens with a numerical aperture of 0.42. The angle-resolved reflectance/PL spectroscopy consists of reflectance/PL spectra for different incidence angle θ, which are performed by projecting the back focal plane of the objective lens to a spectrometer (FHR 640) equipped with a Si charge coupled device (CCD) camera.

Transient angle-resolved reflectance spectroscopy

The tr-ARR measurements are performed with a home-built set-up, which is schematically shown in supplementary Fig. S11. A 1-kHz 800-nm pulsed laser is used as pump light. The pulse width is about 150 fs. The probe light is the white light generated by pumping a sapphire plate with the fs laser. The delay time t between the pump light and the white probe light is precisely controlled to yield the time evolution of $\Delta R/R$. The pump energy density is kept low at 5.1 pJ/μm^2 to avoid compromising the coherence of the exciton-magnon coupling due to high carrier/exciton density. The pump light intensity is modulated at the frequency of 20 Hz and the k-space image of the pump induced reflectance change is dispersed and recorded with an EMCCD camera (from Raptor Photonics) that is synchronized to the modulation speed. The pump and probe light spot size is about 10 μm.

Numerical simulations

The finite element method (FEM) is employed to simulate the eigenvalues and reflectance spectra of CrSBr photonic structures using a commercially available software (COMSOL Multiphysics). Periodic boundary conditions are applied in the x- and y-directions, while perfectly matched layers (PMLs) are implemented in the z-direction to minimize reflections. The optical anisotropy of the material is modeled using a dielectric tensor,

$$\boldsymbol{\varepsilon} = \begin{bmatrix} \varepsilon_a & 0 & 0 \\ 0 & \varepsilon_b & 0 \\ 0 & 0 & \varepsilon_c \end{bmatrix} \tag{2}$$

where $\varepsilon_a = 12$, $\varepsilon_c = 3.7$. To simulate the eigen-energy of polariton bands, the ε_b is approximated with the Lorentzian mode:

$$\varepsilon_b(\omega) = \varepsilon_{b0} + \frac{|f|^2}{E_X^2/\hbar^2 - \omega^2 - i\omega\Gamma} + \frac{|f^*|^2}{E_{X^*}^2/\hbar^2 - \omega^2 - i\omega\Gamma^*} \tag{3}$$

with $\varepsilon_{b0} = 11.1$. The contribution of exciton resonance is taken into account with following parameters, $E_X = 1.364$ eV, $E_{X^*} = 1.379$ eV, $\hbar\Gamma = 0.7$ meV, $\hbar\Gamma^* = 7.5$ meV, $\hbar f = 1.304$ eV, $\hbar f^* = 0.707$ eV. The wave equation,

$$\nabla \times (\nabla \times \mathbf{E}(\omega)) = k_0^2 \boldsymbol{\varepsilon}(\omega)\mathbf{E}(\omega) \tag{4}$$

is then solved numerically by matching the frequency of the eigen mode $\mathbf{E}(\omega)$ with the dielectric function dispersion $\boldsymbol{\varepsilon}(\omega)$.

To simulate the magneto-optical effect, an off-diagonal gyromagnetic term is introduced into the dielectric tensor as[46],

$$= \begin{bmatrix} \varepsilon_a & \varepsilon_{ab} & 0 \\ -\varepsilon_{ab} & \varepsilon_b & 0 \\ 0 & 0 & \varepsilon_c \end{bmatrix} \tag{5}$$

Data availability

The data that support the plots within this paper and other findings of this study are available from the corresponding authors upon reasonable request. The raw data are available via the repository at: https://figshare.com/articles/dataset/Source_data_for_NCOMMS-25-41272B/30938516.

References

1. Wolf, S. A. et al. Spintronics: a spin-based electronics vision for the future. *Science* **294**, 1488–1495 (2001).

2. Žutić, I., Fabian, J. & Das Sarma, S. Spintronics: fundamentals and applications. *Rev. Mod. Phys.* **76**, 323–410 (2004).
3. Manipatruni, S. et al. Scalable energy-efficient magnetoelectric spin–orbit logic. *Nature* **565**, 35–42 (2019).
4. Huang, J. Y. et al. High-fidelity spin qubit operation and algorithmic initialization above 1 K. *Nature* **627**, 772–777 (2024).
5. Zhang, Y. et al. Room temperature field-free switching of perpendicular magnetization through spin-orbit torque originating from low-symmetry type II Weyl semimetal. *Sci. Adv.* **9**, eadg9819 (2023).
6. Dainone, P. A. et al. Controlling the helicity of light by electrical magnetization switching. *Nature* **627**, 783–788 (2024).
7. Javadi, A. et al. Spin–photon interface and spin-controlled photon switching in a nanobeam waveguide. *Nat. Nanotech* **13**, 398–403 (2018).
8. Li, L. et al. Heterogeneous integration of spin–photon interfaces with a CMOS platform. *Nature* **630**, 70–76 (2024).
9. Huang, Y. et al. Room-temperature electron spin polarization exceeding 90% in an opto-spintronic semiconductor nanostructure via remote spin filtering. *Nat. Photonics* **15**, 475–482 (2021).
10. Appel, M. H. et al. Coherent spin-photon interface with waveguide induced cycling transitions. *Phys. Rev. Lett.* **126**, 013602 (2021).
11. Gong, S.-H., Alpeggiani, F., Sciacca, B., Garnett, E. C. & Kuipers, L. Nanoscale chiral valley-photon interface through optical spin-orbit coupling. *Science* **359**, 443–447 (2018).
12. Shreiner, R., Hao, K., Butcher, A. & High, A. A. Electrically controllable chirality in a nanophotonic interface with a two-dimensional semiconductor. *Nat. Photon.* **16**, 330–336 (2022).
13. Chen, Y. et al. Chirality-dependent unidirectional routing of WS2 valley photons in a nanocircuit. *Nat. Nanotechnol.* **17**, 1178–1182 (2022).
14. Mouradian, S. L. et al. Scalable integration of long-lived quantum memories into a photonic circuit. *Phys. Rev. X* **5**, 031009 (2015).
15. Babin, C. et al. Fabrication and nanophotonic waveguide integration of silicon carbide colour centres with preserved spin-optical coherence. *Nat. Mater.* **21**, 67–73 (2022).
16. Kikkawa, J. M., Smorchkova, I. P., Samarth, N. & Awschalom, D. D. Room-temperature spin memory in two-dimensional electron gases. *Science* **277**, 1284–1287 (1997).
17. Herbschleb, E. D. et al. Ultra-long coherence times amongst room-temperature solid-state spins. *Nat. Commun.* **10**, 3766 (2019).
18. Sugano, S., Tanabe, Y. & Kamimura, H. *Multiplets of Transition-Metal Ions in Crystals*. Academic Press, (1970).
19. Seyler, K. L. et al. Ligand-field helical luminescence in a 2D ferromagnetic insulator. *Nat. Phys.* **14**, 277–281 (2018).
20. Szczytko, J., Mac, W., Twardowski, A., Matsukura, F. & Ohno, H. Antiferromagnetic *p*–*d* exchange in ferromagnetic $Ga_{1-x}Mn_xAs$ epilayers. *Phys. Rev. B* **59**, 12935–12939 (1999).
21. Poggio, M., Myers, R. C., Stern, N. P., Gossard, A. C. & Awschalom, D. D. Structural, electrical, and magneto-optical characterization of paramagnetic GaMnAs quantum wells. *Phys. Rev. B* **72**, 235313 (2005).
22. Lu, H. & Long, R. Magnetic structure-dependent ultrafast spin relaxation in magnet CrI3: a time-domain ab initio study. *Nano Lett.* **24**, 8940–8947 (2024).
23. Zhang, X.-X. et al. Gate-tunable spin waves in antiferromagnetic atomic bilayers. *Nat. Mater.* **19**, 838–842 (2020).
24. Lee, K. et al. Magnetic order and symmetry in the 2D semiconductor CrSBr. *Nano Lett.* **21**, 3511–3517 (2021).
25. Dirnberger, F. et al. Magneto-optics in a van der Waals magnet tuned by self-hybridized polaritons. *Nature* **620**, 533–537 (2023).
26. Wang, T. et al. Magnetically-dressed CrSBr exciton-polaritons in ultrastrong coupling regime. *Nat. Commun.* **14**, 5966 (2023).
27. Wilson, N. P. et al. Interlayer electronic coupling on demand in a 2D magnetic semiconductor. *Nat. Mater.* **20**, 1657–1662 (2021).
28. Klein, J. et al. Control of structure and spin texture in the van der Waals layered magnet CrSBr. *Nat. Commun.* **13**, 5420 (2022).
29. Chen, Y. et al. Twist-assisted all-antiferromagnetic tunnel junction in the atomic limit. *Nature* **632**, 1045–1051 (2024).
30. Tabataba-Vakili, F. et al. Doping-control of excitons and magnetism in few-layer CrSBr. *Nat. Commun.* **15**, 4735 (2024).
31. Chumak, A. V., Vasyuchka, V. I., Serga, A. A. & Hillebrands, B. Magnon spintronics. *Nat. Phys.* **11**, 453–461 (2015).
32. Bae, Y. J. et al. Exciton-coupled coherent magnons in a 2D semiconductor. *Nature* **609**, 282–286 (2022).
33. Diederich, G. M. et al. Tunable interaction between excitons and hybridized magnons in a layered semiconductor. *Nat. Nanotechnol.* **18**, 23–28 (2023).
34. Ardizzone, V. et al. Polariton Bose–Einstein condensate from a bound state in the continuum. *Nature* **605**, 447–452 (2022).
35. Zhao, X. et al. Spin-orbit-locking chiral bound states in the continuum. *Phys. Rev. Lett.* **133**, 036201 (2024).
36. Li, Q. et al. Two-dimensional magnetic exciton polariton with strongly coupled atomic and photonic anisotropies. *Phys. Rev. Lett.* **133**, 266901 (2024).
37. Huang, C. et al. Ultrafast control of vortex microlasers. *Science* **367**, 1018–1021 (2020).
38. Wu, X. et al. Exciton polariton condensation from bound states in the continuum at room temperature. *Nat. Commun.* **15**, 3345 (2024).
39. Koshelev, K., Lepeshov, S., Liu, M., Bogdanov, A. & Kivshar, Y. Asymmetric metasurfaces with high-Q resonances governed by bound states in the continuum. *Phys. Rev. Lett.* **121**, 193903 (2018).
40. Liang, Y., Tsai, D. P. & Kivshar, Y. From Local to nonlocal high-Q plasmonic metasurfaces. *Phys. Rev. Lett.* **133**, 053801 (2024).
41. Yuan, Y. et al. Robust purcell effect of $CsPbI_3$ quantum dots using nonlocal plasmonic metasurfaces. *Phys. Rev. Lett.* **134**, 243804 (2025).
42. Bae, Y. J. et al. Transient magnetoelastic coupling in CrSBr. *Phys. Rev. B* **109**, 104401 (2024).
43. Sun, Y. et al. Dipolar spin wave packet transport in a van der Waals antiferromagnet. *Nat. Phys.* **20**, 794–800 (2024).
44. *Spin Physics in Semiconductors*. **157** (Springer International Publishing, 2017).
45. Hopfield, J. J. Theory of the contribution of excitons to the complex dielectric constant of crystals. *Phys. Rev.* **112**, 1555–1567 (1958).
46. Carey, B. et al. Giant Faraday rotation in atomically thin semiconductors. *Nat. Commun.* **15**, 3082 (2024).
47. Estrecho, E. et al. Direct measurement of polariton-polariton interaction strength in the Thomas-Fermi regime of exciton-polariton condensation. *Phys. Rev. B* **100**, 035306 (2019).
48. Feng, J. et al. All-optical switching based on interacting exciton polaritons in self-assembled perovskite microwires. *Sci. Adv.* **7**, eabj6627 (2021).

Acknowledgements

This work was financially supported by the National Key Research and Development Program of China (No. 2022YFA1405100, 2024YFB3612800, 2024YFA1409700), the National Natural Science Foundation of China (No. 92577126,12374077, 12174384, 12241405, 12174378, 12274406, 12427805), CAS Project for Young Scientists in Basic Research (No. YSBR-120), the Beijing Natural Science Foundation Key Program (No. Z220005).

Author contributions

Y.H. and K.W. conceived and coordinated the project. Q.H. fabricated the device and performed structure characterization under the supervision of Y.H. and K.W. Q.H., Y.H. performed steady-state and ultrafast optical spectroscopy experiments and analyzed the data with the help of J.F., A.F. and K.W. J.F. provided the simulation of the photonic structure.

H.W., X.Z., W.Z., N.J., X.Q., and J.Z. assisted in sample preparation and measurements. Y.J. and D.S. contributed to scientific discussions. Q.H., Y.H. and K.W. wrote the manuscript. All authors reviewed and edited the manuscript.

Competing interests

The authors declare no competing interest.

Additional information

Supplementary information The online version contains supplementary material available at https://doi.org/10.1038/s41467-026-68767-9.

Correspondence and requests for materials should be addressed to Yuqing Huang, Jiangang Feng or Kaiyou Wang.

Peer review information Nature Communications thanks the anonymous reviewer(s) for their contribution to the peer review of this work. A peer review file is available.

Reprints and permissions information is available at http://www.nature.com/reprints

Publisher's note Springer Nature remains neutral with regard to jurisdictional claims in published maps and institutional affiliations.

Open Access This article is licensed under a Creative Commons Attribution-NonCommercial-NoDerivatives 4.0 International License, which permits any non-commercial use, sharing, distribution and reproduction in any medium or format, as long as you give appropriate credit to the original author(s) and the source, provide a link to the Creative Commons licence, and indicate if you modified the licensed material. You do not have permission under this licence to share adapted material derived from this article or parts of it. The images or other third party material in this article are included in the article's Creative Commons licence, unless indicated otherwise in a credit line to the material. If material is not included in the article's Creative Commons licence and your intended use is not permitted by statutory regulation or exceeds the permitted use, you will need to obtain permission directly from the copyright holder. To view a copy of this licence, visit http://creativecommons.org/licenses/by-nc-nd/4.0/.

© The Author(s) 2026